Journal of Photochemistry & Photobiology, A: Chemistry 447 (2024) 115252

Contents lists available at ScienceDirect

Journal of Photochemistry & Photobiology, A: Chemistry

journal homepage: www.elsevier.com/locate/jphotochem

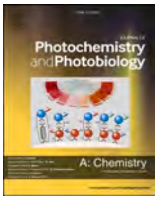

A novel Z-scheme heterojunction Fe-BDC/TiO_2 for efficient photocatalytic degradation of acetaldehyde

Hongyun Xue [a], Gansheng Shi [a], Guanhong Lu [a], Xinhong Xu [b,*], Xiaomeng Ren [b], Yan Wang [a,*], Xiao Wang [a], Xiaofeng Xie [a], Jing Sun [a]

[a] State Key Lab of High Performance Ceramics and Superfine Microstructure, Shanghai Institute of Ceramics, Chinese Academy of Sciences, 585 Heshuo Road, Shanghai 201899, China

[b] Navy Medical Centre, 880 Xiangyin Road, Shanghai 200433, China

A R T I C L E I N F O

Keywords:
Photodegradation acetaldehyde
Fe-BDC
TiO_2
Heterojunction

A B S T R A C T

Constructing heterojunction structures is considered one of the effective methods to improve the activity of photocatalysts. A novel Z-Scheme heterojunction Fe-BDC/TiO_2 was designed and synthesized by amorphous gel Fe-BDC and TiO_2 nanoparticles with electrostatic self-assembly method. The introduction of Fe-BDC has been proved to expand the light absorption range and promote the separation and transfer of interface photo generated electrons and holes. Thus, the photocatalytic degradation efficiency of acetaldehyde by 5% Fe-BDC/TiO_2 sample is 2.3 times than that of pure TiO_2 sample. And the reaction rate is 2.5 times than that of pure TiO_2 sample. The free radical capture experiment shows that $\bullet O_2^-$ played a more important role in the degradation of acetaldehyde. In addition, in situ infrared analysis further reveals the surface species of the photocatalysts during adsorption and degradation processes. The acetaldehyde degradation route of Fe-BDC/TiO_2 has been speculated. ‘1These findings provide valuable references for the design of metal oxide semiconductor/Fe based MOF heterojunctions and the efficient degradation of aldehyde VOCs.

1. Introduction

Volatile organic compounds (VOCs), such as benzene compounds, aldehydes, alcohols, and ketones, are considered the main pollutants in the atmospheric environment [1]. VOCs can also be involved in the formation of ozone and secondary aerosols, which is an important precursor of $PM_{2.5}$ [2] (Particulate Matter with diameter less than 2.5 μm). Moreover, most VOCs have toxic, irritating, teratogenic and carcinogenic [3,4]. Photocatalytic oxidation technology, as a green, cost-effective and efficient technology, can degrade typical VOCs under mild conditions [5,6]. Titanium dioxide (TiO_2) is a widely used photocatalyst to photodegrade various VOCs due to its low cost and non-toxicity [7,8]. However, due to the easy recombination of photo generated charge carriers, the catalytic degradation efficiency of TiO_2 is low.

Researchers have effectively promoted the separation of photo generated electron hole pairs through appropriate design of photocatalysts, such as doping, metal loading, and the introduction of heterojunctions [9–11]. Among the proposed strategies, the introduction of heterojunctions is one of the most promising methods for preparing efficient photocatalysts [12,13]. Metal organic frameworks (MOFs) are porous materials composed of metal ions/clusters and bridged organic ligands [14,15]. MOF has the advantages of high porosity, large specific surface area, adjustable structure, and many active sites [16,17]. It has great application potential in sensing, gas storage, separation, catalysis and other fields [18–21].

In the large family of MOF materials, iron based MOFs have attracted much attention due to their low cost, environmental protection, and unique physical and chemical properties [22,23]. Iron based MOFs also show great potential in heterogeneous photocatalysts or photo Fenton catalysts because of its highly ordered structure, non-toxic characteristics and the ability to absorb visible light [24]. In addition to the common crystalline Fe-based MOF (such as MIL-101 (Fe)), an amorphous gel like Fe-BDC has also attracted the attention of researchers. It has the main common feature with MIL-101 (Fe): the same 2θ XRD reflection of position, similar thermal stability, almost identical junction conformation, etc.[25]. In addition, its synthesis can utilize solvent regulation deprotonation under room temperature and pressure [26].

---

* Corresponding authors.
E-mail addresses: xxh2748@163.com (X. Xu), wangyan@mail.sic.ac.cn (Y. Wang).

https://doi.org/10.1016/j.jphotochem.2023.115252
Received 2 August 2023; Received in revised form 25 September 2023; Accepted 8 October 2023

In this work, we constructed a Fe-BDC/TiO_2 heterojunction structure and characterized its phase structure, morphology, light absorption, and chemical composition. And explore its adsorption and degradation ability for aldehyde VOCs through photocatalytic degradation experiments. In addition, the separation and transfer of photo generated electron-hole pairs in Fe-BDC/TiO_2 heterojunction structures has been studied through steady-state fluorescence spectroscopy, photocurrent response, and electrochemical impedance. Combining VB-XPS and band gap to explore the type of heterostructure. The experiment also explores the role of different free radicals in the degradation of acetaldehyde and the pathway of acetaldehyde degradation. This work could provide valuable reference for the design of metal oxide semiconductor/Fe based MOF heterojunctions and the efficient degradation of aldehyde VOCs.

2. Experimental

2.1. Chemicals and materials

Anatase TiO_2 was purchased from Aladdin Industries Corporation. Ferric chloride hexahydrate ($FeCl_3{\cdot}6H_2O$), N,N-dimethylformamide (DMF, AR) and 1,4-terephthalic acid (H_2BDC) were purchased from Shanghai adamas Reagent Co., Ltd. Triethylamine (TEA, AR) was purchased from Sinopharm Chemical Reagent Co., Ltd. Absolute ethanol was supplied by Sinopharm Chemical Reagent Co., Ltd. Deionized (DI) water was produced by ultrapure water machine (Tondino Scientific (Shanghai) Co., Ltd). All chemicals used in our study without further purification.

2.2. The synthesis of Fe-BDC/TiO_2

According to the literature, amorphous gel Fe-BDC was synthesized at room temperature and pressure [27]. 1 mmol $FeCl_3{\cdot}6H_2O$ was dissolved in 50 mL DMF. 1 mmol H_2BDC, 4 mL of ethanol,4 mL of deionized water and 1.5 mL TEA were added into the Fe-DMF solution under stirring, respectively. After 12 h, a uniform colloidal suspension was collected by centrifuging at 8000 rpm (5 min) and washed 3 times with ethanol. Finally colloidal substance was freeze-dried to obtain Fe-BDC.

An appropriate amount of Fe-BDC was ultrasonically dispersed in 30 mL deionized water and TiO_2 nanoparticles were added. After stirring 6 h, Fe-BDC/TiO_2 were successfully prepared by electrostatic self-assembly method. After that, the mixed suspension was centrifuged and dried. The samples were named as x% FT, where the x% represented the mass percentage of Fe-BDC.

2.3. Characterization

X-ray diffraction (XRD) were collected by high-resolution powder X-ray diffractometer (BRUKER AXS GMBH, D8 DISCOVER DAVINCI) using Cu Ka radiation (λ = 0.15418 nm) with 2θ varied from 3° to 80° (5°/min). UV–vis spectra were carried out by Shimadzu UV-3600 spectrometer. Photoluminescence spectra were supplied by fluorescence spectrophotometer (Edinburgh Instruments FLSP-920) with an excitation wavelength of 250 nm. The Brunauer–Emmett–Teller (BET) tests were measured by Micromeritics nitrogen adsorption apparatus (ASAP3000). X-ray photoelectron spectroscopy (XPS) and valance band XPS (VB-XPS) experiments were carried out using a twin anode gun, Mgka (1253.6 eV) (Microlab 310F scanning Auger microprobe, Thermo Fisher Scientific, ESCAlab250). Photocurrent measurement was performed on CHI 660 electrochemical analyzer with the samples as the working electrode, the platinum sheet as the counter and the saturated calomel as the reference electrode. The electrolyte was 0.2 mol/L Na_2SO_4 solution. In situ Diffuse Reflection Infrared Fourier Transform spectroscopy (DRIFTS) was carried out on the Shimadzu IRTracer-100 instrument with a mercury cadmium telluride (MCT) detector to monitor the intermediates in the photocatalytic degradation of acetaldehyde.

2.4. Photocatalytic performance testing

In this work, to evaluate the performance of as-prepared photocatalysts, the target pollutant is acetaldehyde in a continuous flow reactor system. 250 W xenon lamp (light intensity 204 W/m^2) was used as the light source. 50 mg as-prepared photocatalyst was dispersed in ethanol by ultrasonication and then coated on a glass plate. The flowrate of gas mixture (acetaldehyde: air = 1:1) was set at 20 standard cubic centimeters per minute (sccm). The initial concentration of gaseous acetaldehyde was 500 ppm and the change of concentration was recorded in real-time by gas chromatography (GC). Saturated adsorption capacity (A, μMol/g) is calculated using the following expression:

$$A=\{C_0 \times \rho_0 \times \rho_1\times[(\int_0^t \nu \times Cdt)blank - (\int_0^t \nu \times Cdt)sample]\}/(M \times m).$$

Among them, C_0 (ppm) and C (ppm) are the initial concentration and real-time concentration, respectively. ρ_0 (g/cm^3) and ρ_1 (g/cm^3) represents the density of air and VOCs relative vapor density at room temperature respectively. t (min) is the time point of data recording, υ (mL/min) is the flow rate of the mixed gas. M (g/mol) and m (g) are the molar mass of VOCs and mass of photocatalyst, respectively. The photodegradation efficiency of gaseous acetaldehyde was calculated by:

$$X = (C_0\text{-}C)/C_0 \times 100\ \%$$

The mineralization rate of gaseous acetaldehyde was determined by:

$$\eta = \triangle[CO_2]/[2 \times (C_0\text{-}C)] \times 100\ \%$$

$\triangle[CO_2]$ is the outlet CO_2 concentration, [2× (C_0-C)] represents the theoretical yield of CO_2 generated during the complete oxidation of acetaldehyde.

ESR test: Firstly, 4 mg of the sample was dispersed in 2 mL of ethanol. Next, 100 μL solution and 30 μL DMPO (Dimethylpyridine N-oxide) were mixed thoroughly and then irradiated under xenon lamp for 5 min. Finally, a certain amount of mixed solution was put into the EPR sample chamber to detect hydroxyl radicals and superoxide radicals.

Free radical capture experiment: TEMPO (2,2,6,6-Tetramethylpiperidinooxy) and PBQ (p-benzoquinone) were used as hydroxyl radical and superoxide radical quenching agents respectively. The TEMPO (or PBQ) and sample were dispersed in ethanol solution at a ratio of 1:10 and coated on glass plate. The next steps were consistent with the photocatalytic testing method.

3. Results and discussion

As shown in Fig. 1a, TiO_2 sample shows characteristic peaks of anatase type: 25.4° (1 0 1), 37.8° (0 0 4), 48.1° (2 0 0), 53.9° (1 0 5), 55.1° (2 1 1), 62.7° (2 0 4), 68.7° (1 1 6), 70.3° (2 2 0) and 75.1° (2 1 5) [28]. As shown in S1, Fe-BDC exhibits amorphous structure with its peak located at 2θ = 8.3° and 17.4°, corresponding to the (2 0 0) and (4 0 0) planes of their monoclinic structure. The Fe atom is coordinated by six O atoms (μ_3-OH and O in carboxylates) to form slightly twisted FeO_6 octahedra, which is further connected by corners/edges in the (2 0 0) plane [29]. Because amorphous gel Fe-BDC has low crystallinity and low peak strength, the composite only displayed TiO_2 characteristic peaks.

The utilization of light is the key factor to determining the performance of photocatalysts. The UV–vis spectra of TiO_2 and Fe-BDC/TiO_2 were showed in Fig. 1b. TiO_2 can absorb ultraviolet light, while Fe-BDC has a wider range of light absorption. As the Fe-BDC content in the composite material increasing, the light absorption edge of x% Fe-BDC/TiO_2 composites show a slightly red shift. The bandgap values corresponding to TiO_2, 2 % Fe-BDC/TiO_2, 5 % Fe-BDC/TiO_2, 10 % Fe-BDC/TiO_2, and Fe-BDC are 3.13 eV, 3.09 eV, 2.99 eV, 2.86 eV, and 2.35 eV, respectively (Fig. S2).

In order to further verified the interface interaction between TiO_2 and Fe-BDC, the chemical composition and binding energy of the material were determined by X-ray photoelectron spectroscopy (XPS). As shown in Fig. 1c, the peak at 725.2 eV could be attributed to the peaks Fe

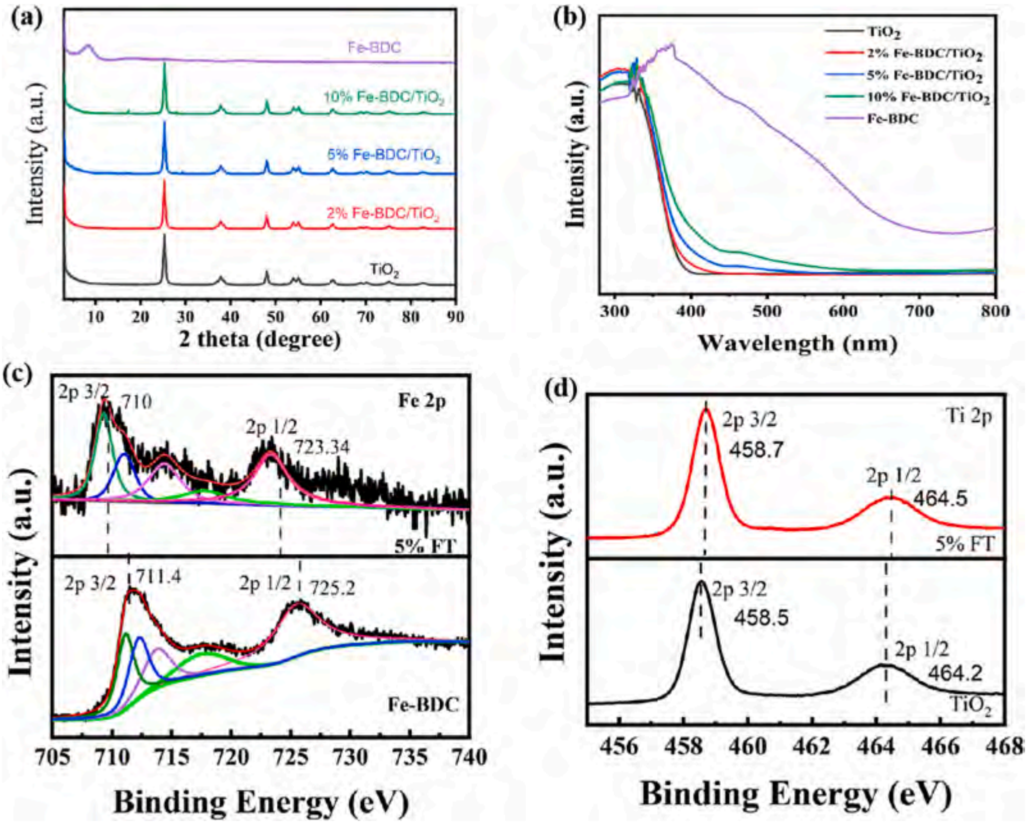

Fig. 1. (a) XRD patterns of TiO_2, 2% Fe-BDC/TiO_2, 5% Fe-BDC/TiO_2, 10% Fe-BDC/TiO_2 and Fe-BDC. (b) UV–vis diffuse reflectance spectroscopy of TiO_2, 2% Fe-BDC/TiO_2, 5% Fe-BDC/TiO_2 and 10% Fe-BDC/TiO_2. (c) Fe 2p spectra of Fe-BDC and 5% Fe-BDC/TiO_2; (d) Ti 2p spectrum of TiO_2 and 5% Fe-BDC/TiO_2.

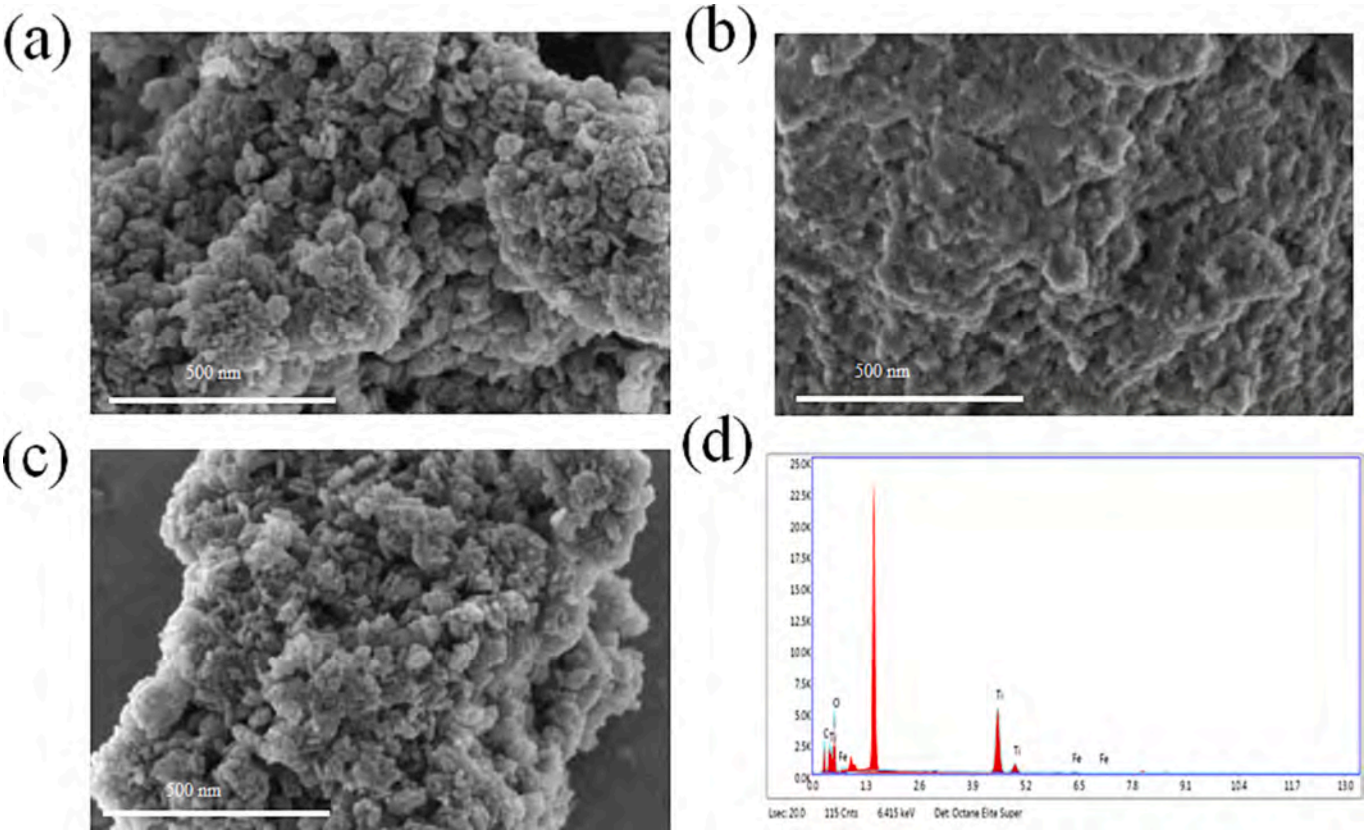

Fig. 2. SEM images of (a) TiO_2, (b) Fe-BDC and (c) 5% Fe-BDC/TiO_2. (d) The EDS mapping of 5% Fe-BDC/TiO_2 sample.

2p1/2. The peak at 711.4 eV represented of Fe 2p3/2, which is decomposed into four peaks located at 717.5, 713.7, 712.2 and 711.1 eV, indicating the coexistence of $Fe^{3+}$and Fe^{2+}[30,31]. In addition, the Fe 2p peak in 5 % Fe-BDC/TiO_2 moves towards low binding energy. The Ti 2p XPS spectrum (Fig. 1d) shows the peaks of Ti 2p1/2 and Ti 2p3/2 at 464.2 eV and 458.5 eV, respectively. The peak of the composites moves towards high binding energy, indicating that the electron cloud density near the Ti-O bond decreased. The O1s spectrum of 5 % Fe-BDC/TiO_2 could be fitted by two splitting peaks near 531.3 and 529.9 eV (Fig. S3), which may be attributed to the carbon oxygen bond (O = C-O) and the Me-O bond (Me: Ti, Fe) in the terephthalic acid linker, respectively [32]. The XPS results indicates that there is a strong interaction between TiO_2 and Fe-BDC, which is conducive to charge transfer [33].

To elucidate the morphology of the sample, the SEM results of TiO_2, Fe-BDC and 5 % Fe-BDC/TiO_2 are illustrated in Fig. 2. The morphology of TiO_2 sample is composed with a large number of aggregated nanoparticles, which forms mesoporous/macroscopic stacking pores. Fe-BDC shows dry gel state with relatively flat surface and small pores. Compared to Fe-BDC, 5 % Fe-BDC/TiO_2 does not show significant changes in morphology due to the small amount. But the agglomeration of TiO_2 particles in 5 % Fe-BDC/TiO_2 is more obviously. The EDS spectrum of 5 % Fe-BDC/TiO_2 was shown in Fig. 2d, where Ti, O, C, and Fe elements are detected. Fe and C elements come from Fe-BDC. Ti element comes from TiO_2. Thus, these results indicate the successful combination of Fe-BDC and TiO_2.

The nitrogen adsorption desorption isotherm of TiO_2, 5 % Fe-BDC/TiO_2 and Fe-BDC are shown in Fig. 3a. Both TiO_2 and 5 % Fe-BDC/TiO_2 exhibit an IV type curve characterized by H2 type hysteresis loops, which indicates the presence of mesopores. Fe-BDC exhibits an IV type curve characterized by H3 type hysteresis loops. Fig. 3b shows the pore size distribution of the three samples. TiO_2 particles irregularly stack to form a mesoporous structure of 10–20 nm. Fe-BDC has hierarchical structure of micropores and mesopores. The 5 % Fe-BDC/TiO_2 had smaller pore size compares to that of pure TiO_2 sample, which may attribute to the intensification of TiO_2 particle aggregation during the synthesis process. Despite the relatively higher specific surface areas of Fe-BDC (134.39 m^2/g) and TiO_2 (92.3 m^2/g), the specific surface area of 5 % Fe-BDC/TiO_2 decreased to 79.46 m^2/g, which might be attributed to the aggregation of TiO_2 particles in the electrostatic self-assembly process of the two components. The relatively lower specific surface area of 5 % Fe-BDC/TiO_2 results in a weak adsorption capacity.

The capture of VOCs is the first step in the photocatalytic oxidation of gaseous pollutants. Thus, the adsorption capacity of as-prepared photocatalysts for gaseous acetaldehyde was characterized under dark condition as shown in Fig. 3c and 3d. The adsorption amount of TiO_2 for acetaldehyde is 50.01 μmol/g, while that of 5 % Fe-BDC/TiO_2 decreases to 30.33 μmol/g. The results are consistent with that of specific surface area.

The photodegradation curve of flowing gaseous acetaldehyde are shown in Fig. 4a. It can be found that all the Fe-BDC/TiO_2 photocatalysts have better photocatalytic performance than that of pure TiO_2. The degradation efficiency of acetaldehyde by different photocatalysts are as follows: 5 % Fe-BDC/TiO_2 (44.6 %) > 10 % Fe-BDC/TiO_2 (35.5 %) > 2 % Fe-BDC/TiO_2 (32.4 %) > TiO_2 (19.1 %). The photocatalytic degradation efficiency of acetaldehyde by 5 % Fe-BDC/TiO_2 is 2.3 times that of pure TiO_2 sample. The reaction rates (min^{-1}) of 5 % Fe-BDC/TiO_2, 10 % Fe-BDC/TiO_2, 2 % Fe-BDC/TiO_2 and TiO_2 are 0.00840, 0.00644, 0.00584 and 0.00329, respectively (Fig. 4b). The reaction rate of the 5 % Fe-BDC/TiO_2 is about 2.5 times that of pure TiO_2 sample. Compared to pure TiO_2 and other composites, 5 %FT shows the lowest PL intensity (Fig. 5a), confirming the efficient charge transfer between the two components, which inhibit the electron-hole recombination and promote the generation of highly oxidative radicals, leading to an increase in the photocatalytic performance. Interestingly, when further increase the amount of Fe-BDC to 10 %, the PL intensity of the sample increased, together with a decrease in the photo-catalytic performance. On one hand, the amount of TiO_2 in 10 %FT is lower than 5 %FT, which limited the amount of photo-induced electrons and the generation of highly oxidative$\cdot O_2^-$ radicals. On the other hand, the introduction of Fe-BDC lead to the aggregation of TiO_2 and results in a decrease in composite uniformity, which, together with the excitation of Fe-BDC, might explain the increased PL intensity of 10 %FT. Besides, the aggregation of

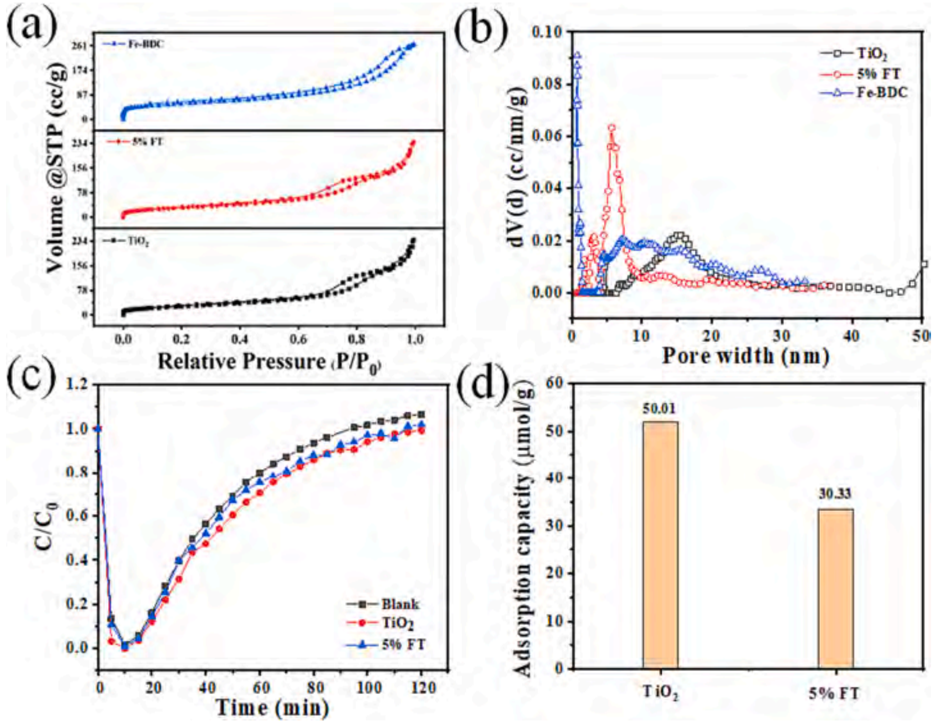

Fig. 3. (a) N_2 adsorption–desorption isotherms at 77 K and (b) pore size distribution of TiO_2, 5 % Fe-BDC/TiO_2 and Fe-BDC; (c) Dynamic adsorption curve for gaseous acetaldehyde under dark conditions and (d) adsorption capacity histogram of TiO_2 and 5 % Fe-BDC/TiO_2.

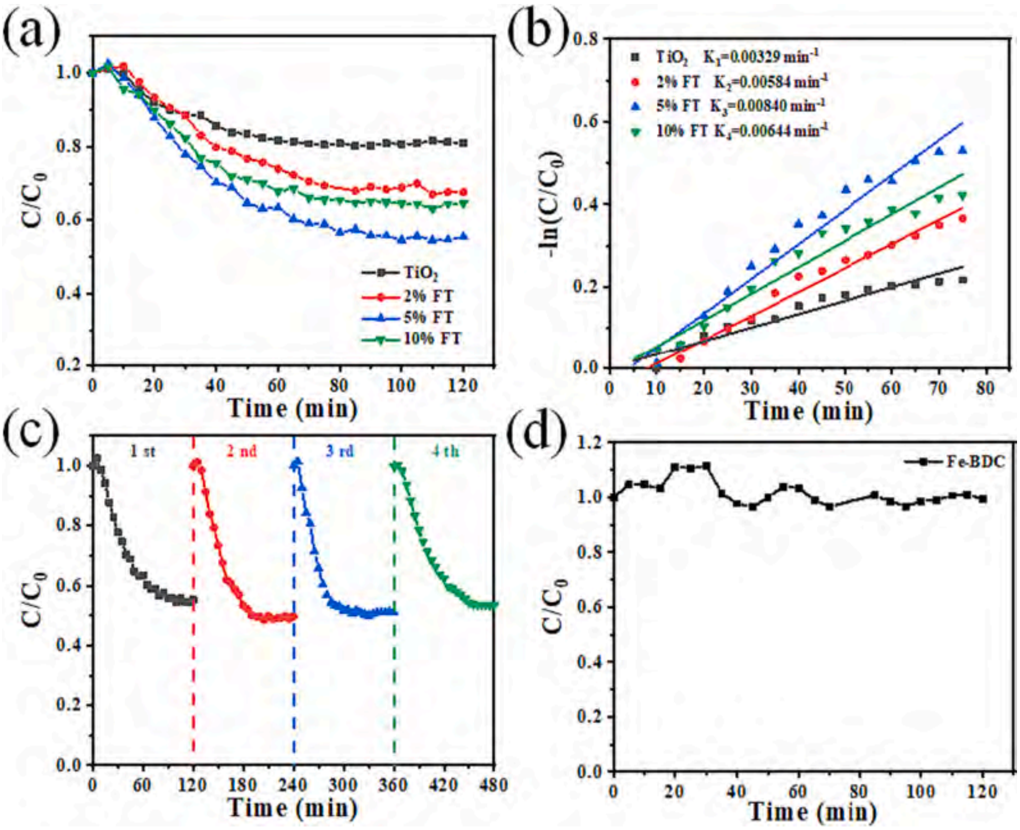

Fig. 4. (a) Catalytic degradation curves of gaseous acetaldehyde under 250 W xenon lamp irradiation and (b) Kinetic model of acetaldehyde photocatalytic degradation rate of TiO_2, 2 % Fe-BDC/TiO_2, 5 % Fe-BDC/TiO_2 and 10 % Fe-BDC/TiO_2; (c) Degradation curve of 5 % Fe-BDC/TiO_2 in four cycles; (d) Photocatalytic degradation curve of Fe-BDC on gaseous acetaldehyde.

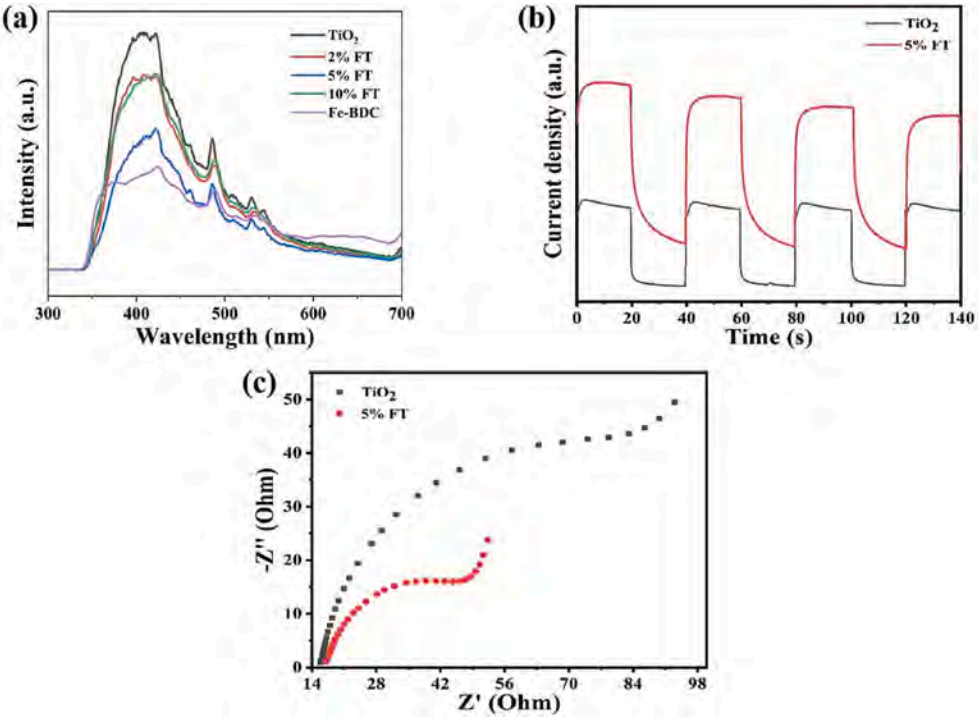

Fig. 5. (a) PL spectra of Fe-BDC, Fe-BDC/TiO_2 samples and TiO_2, (b) photocurrent response curves and (c) EIS curves of 5% Fe-BDC/TiO_2 and TiO_2.

TiO_2 is detrimental for the adsorption capacity of FT samples, which also caused a decrease in the photo-catalytic performance of 10 %FT. In order to test the stability of the composite photocatalysts, we conducted a cycle experiment with 5 % Fe-BDC/TiO_2 (Fig. 4c). After four cycles, the photodegradation efficiency of 5 % Fe-BDC/TiO_2 stabilized to approximately 35 %. Fig. 4d shows that the acetaldehyde concentration is stable in the Fe-BDC photocatalysis process. Thus, Fe-BDC cannot photodegrade gaseous acetaldehyde under this condition, which is possibly due to its mismatch of energy bands.

The intensity of PL emission peak reflects the recombination rate of photo generated electron hole pairs. As shown in Fig. 5a, the PL peak intensity of TiO_2 is stronger than that of 5 % Fe-BDC/TiO_2. It may be due to the formation of heterojunction structure in Fe-BDC/TiO_2, which can promote charge transfer and effectively suppressing the recombination of photo generated electron hole pairs between TiO_2 and Fe-BDC. Subsequently, the response of the photocatalyst to light is studied through photocurrent testing. Fig. 5b shows the photocurrent density of TiO_2 and 5 % Fe-BDC/TiO_2 over three cycles. Obviously, 5 % Fe-BDC/TiO_2 has higher photocurrent density with higher efficiency in separating photo generated carriers than that of TiO_2. Electrochemical impedance spectroscopy (EIS) is always used to further investigate the surface charge transfer of photocatalysts. The results of the EIS Nyquist plot were shown in Fig. 5c. Compared with pure TiO_2 sample, 5 % Fe-BDC/TiO_2 shows lower arc radius, indicating its lower resistivity. It means that the introduction of Fe-BDC is conducive to promoting charge transfer at the interface between Fe-BDC and TiO_2 and effective separation of photo generated electron hole pairs.

ESR technology was used to monitor specific free radicals generated on TiO_2 and 5 % Fe-BDC/TiO_2. Under xenon lamp irradiation, typical six peak signals of DMPO-$^{\bullet}O_2^-$ and typical four peak signals of DMPO-·OH are detected on TiO_2 and 5 % Fe-BDC/TiO_2 (Fig. 6). Both $^{\bullet}O_2^-$ and $^{\bullet}OH$ are strong oxidants for the catalytic oxidation of acetaldehyde. Due to the improvement of electron hole migration efficiency, the concentration of $^{\bullet}O_2^-$ and $^{\bullet}OH$ generated on 5 % Fe-BDC/TiO_2 is higher than that of pure TiO_2 sample. Therefore, 5 % Fe-BDC/TiO_2 exhibits better acetaldehyde oxidation efficiency.

The energy band structure of semiconductor photocatalyst is a key factor affecting its activity. These influencing factors can further explain the degradation mechanism of acetaldehyde and the charge transfer pathway in the photocatalytic process. According to the VB-XPS spectrum (Fig. 7), the E_{VB} of TiO_2 and Fe-BDC are 2.36 eV and 2.48 eV, respectively. According to DRS and empirical equation $E_{CB} = E_{VB}\text{-}E_g$ calculation, the conduction band potentials of TiO_2 and Fe-BDC are -0.77 eV and 0.13 eV, respectively. ESR testing has confirmed that the composite material Fe-BDC/TiO_2 can generate $^{\bullet}O_2^-$ and $^{\bullet}OH$ simultaneously under xenon lamp irradiation. Therefore, the charge transfer at the material interface follows the Z-type heterojunction mechanism [34,35]. The photogenerated electrons generated by Fe-BDC is excited by light transition to the conduction band and then recombined with the photogenerated holes on the valence band of TiO_2. The strong reducing photogenerated electrons retained in the conduction band of TiO_2 could reduce O_2 to $^{\bullet}O_2^-$. The photo generated holes with strong oxidation ability in the valence band of Fe-BDC could oxidize surrounding H_2O molecules into $^{\bullet}OH$.

The free radical capture experiment can indirectly prove the influence of $^{\bullet}O_2^-$ and $^{\bullet}OH$ in photodegradation acetaldehyde. As shown in Fig. S4, after the addition of TEMPO and PBQ, the degradation efficiency of the catalyst for gas-phase acetaldehyde decreases from 44.6 % to 28.6 % and 12.3 %, respectively. This confirms that $^{\bullet}O_2^-$ and $^{\bullet}OH$ are active species in the photocatalytic degradation of acetaldehyde. Meanwhile, it could also be noted that the addition of PBQ has a higher impact on the degradation of acetaldehyde, indicating that $^{\bullet}O_2^-$ was the main active species for degrading acetaldehyde.

In-situ DRIFTS was used to monitor the intermediates in the photocatalytic degradation of acetaldehyde by TiO_2 and 5 % Fe-BDC/TiO_2. Before the adsorption and degradation of acetaldehyde, the background of the sample in situ DRIFTS was deducted. As shown in Fig. 8a and Table S1, the peaks at 2326, 2372 cm^{-1} (antisymmetric stretching vibration of C = O in CO_2), 3618 cm^{-1} (stretching vibration of O-H), and 3722 cm^{-1} (free water) on the TiO_2 surface indicates the adsorption of CO_2 and H_2O molecules on the surface. The peak of 1647,1700 cm^{-1} appears during the adsorption process corresponding to the stretching vibration of C = O (ν(C = O)), indicating the adsorption of acetaldehyde molecules on the catalyst surface. The peak at 1180 cm^{-1} corresponds to the ν(C-O) in ether and 1373 cm^{-1} corresponds to δs (CH_3) in crotonaldehyde, indicating that chemical reaction has occurred between the aldehyde molecules adsorbed on the surface of TiO_2[36]. After the adsorption reaction of TiO_2 reached equilibrium, xenon lamp was turned on for photocatalytic degradation of acetaldehyde. New peaks at 1550 cm^{-1} ν_{as} (COO) and 1458 cm^{-1} (δ(CH_2)) appears, indicating that acetaldehyde molecules are oxidized into intermediate products such as acetic acid and formic acid during the degradation process. Observing Fig. 8b and combining with Table S2, the species analysis on the 5 % Fe-BDC/TiO_2 surface is similar to that of pure TiO_2 sample. As the reaction time prolonged, the intensity of these peaks gradually increases, indicating that the intermediates accumulate on the surface area of the catalyst. It is worth noting that the peaks intensity of CO_2 and H_2O significantly increase, further confirming that acetaldehyde molecules finally oxidized to CO_2 and H_2O. Combining in situ DRIFTS and previous studies, the possible pathways of acetaldehyde degradation were shown in Fig. 8c [37]. Acetaldehyde may be directly oxidized by $^{\bullet}O_2^-$ or $^{\bullet}OH$ to the final product, or first oxidized by reactive oxygen species to intermediates such as acetic acid and formic acid, and then further thoroughly oxidized by CO_2 and H_2O.

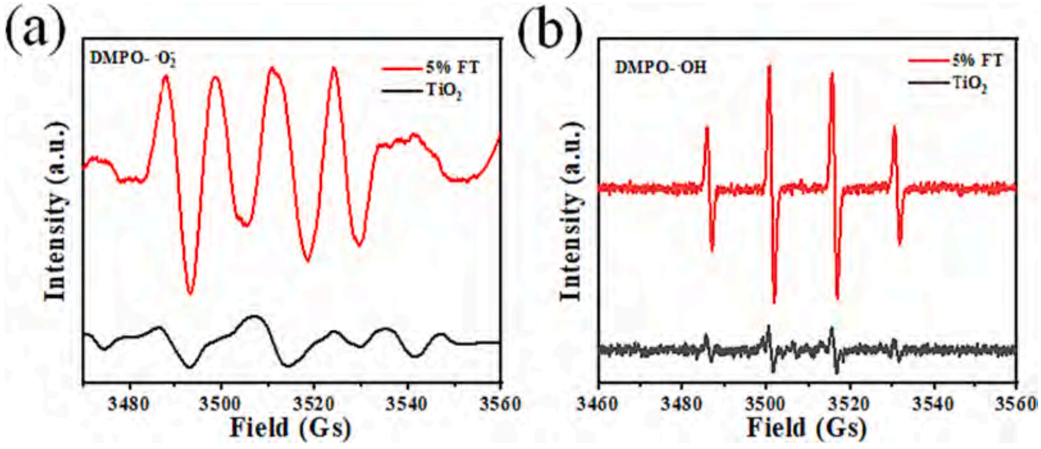

Fig. 6. DMPO spin-trapping ESR spectra of (a) radical $^{\bullet}O_2^-$ (b) radical $^{\bullet}OH$ of TiO_2 and 5% Fe-BDC/TiO_2.

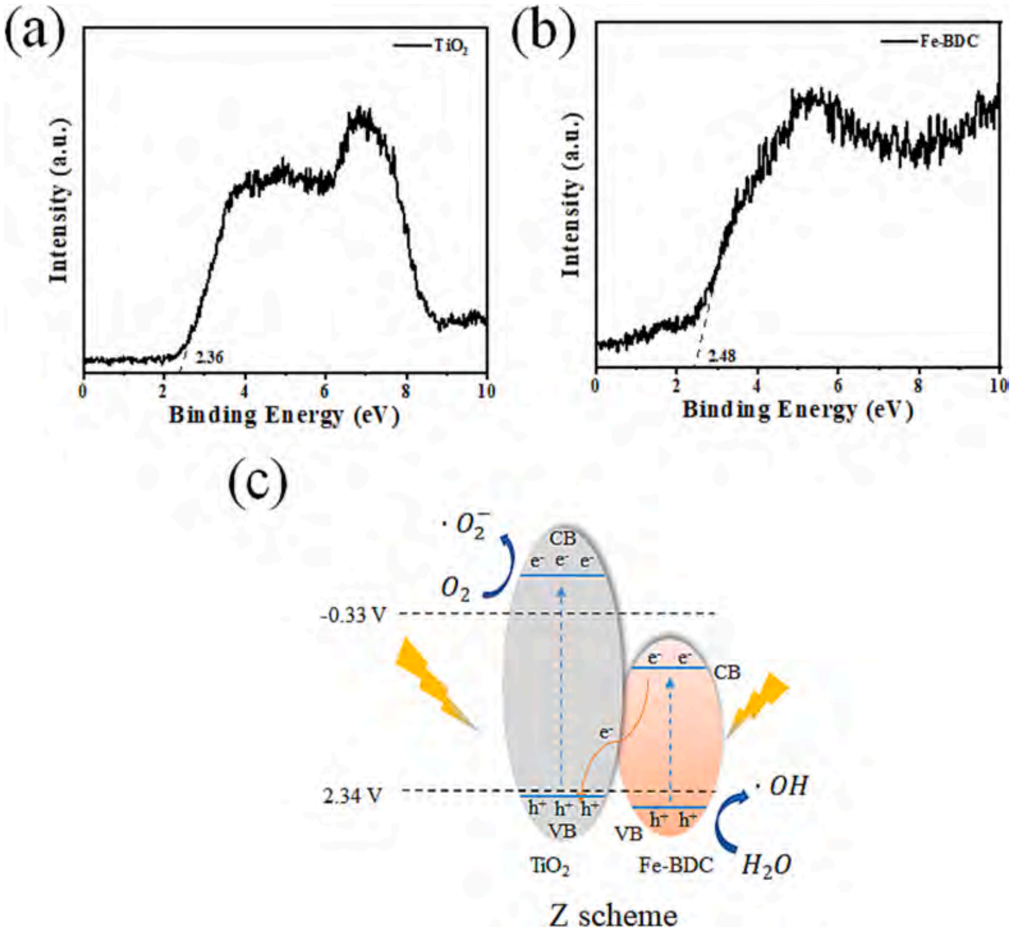

Fig. 7. XPS valence band spectra estimated by (a) TiO_2 and (b) Fe-BDC; (c) Possible charge transfer path between Fe-BDC/TiO_2.

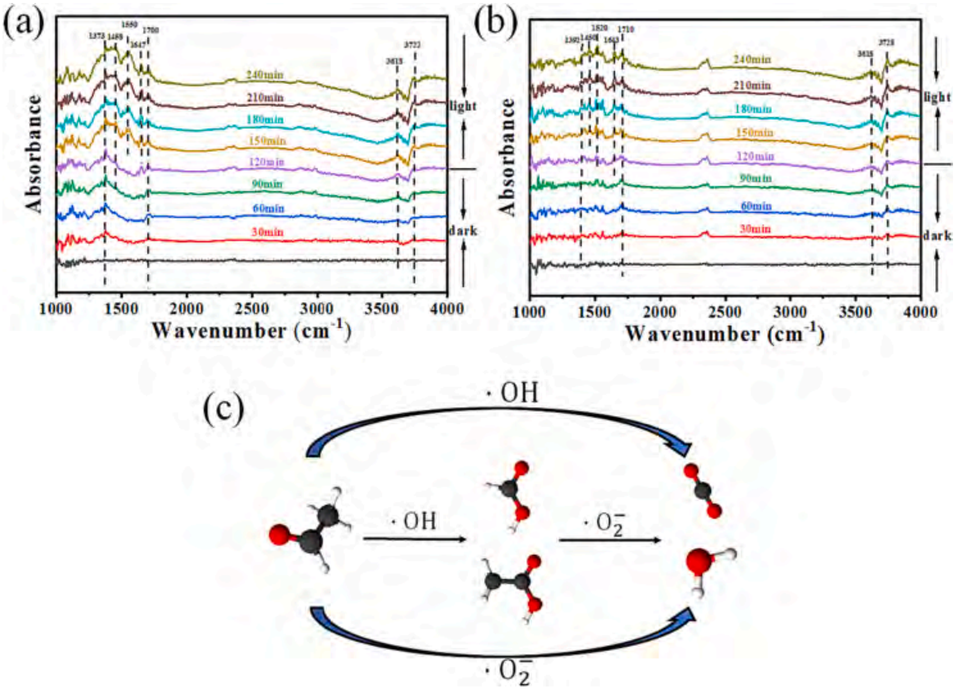

Fig. 8. (a) In situ DRIFTS spectra of TiO_2 and (b) 5% Fe-BDC/TiO_2 photocatalyst for degradation of gaseous acetaldehyde under xenon lamp irradiation. (c) Photocatalytic reaction path of acetaldehyde on catalyst surface.

4. Conclusions

In summary, Fe-BDC/TiO_2 heterojunction has been designed and first applied to photodegrade gaseous acetaldehyde in the mobile phase. The photocatalytic degradation efficiency of acetaldehyde by 5 % Fe-BDC/TiO_2 is 2.5 times that of pure TiO_2 sample. The UV–vis spectrum indicates that the light absorption range of Fe-BDC/TiO_2 increased compared to TiO_2. Through the testing and calculation of band structure and free radical capture experiments, it is further confirmed that the Fe-BDC/TiO_2 formed Z-type heterojunction, promoting the separation and transfer of interface photogenerated electrons and holes, thereby improving the photocatalytic degradation ability. At the same time, the appropriate energy band structure could generate $\cdot O_2^-$ or •OH, where $\cdot O_2^-$ plays a more important role in the degradation of acetaldehyde. In situ infrared spectroscopy reveals the degradation pathway of acetaldehyde. During the degradation of acetaldehyde, intermediate products such as acetic acid and formic acid are formed. These findings provide a way to design efficient heterojunction catalysts and a reference for the photocatalytic oxidation degradation mechanism of gaseous acetaldehyde.

CRediT authorship contribution statement

Hongyun Xue: Writing – original draft. **Gansheng Shi:** Data curation. **Guanhong Lu:** Formal analysis. **Xinhong Xu:** Project administration. **Xiaomeng Ren:** Formal analysis. **Yan Wang:** Writing – review & editing. **Xiao Wang:** Formal analysis. **Xiaofeng Xie:** Formal analysis. **Jing Sun:** Writing – review & editing.

Declaration of Competing Interest

The authors declare that they have no known competing financial interests or personal relationships that could have appeared to influence the work reported in this paper.

Data availability

Data will be made available on request.

Acknowledgments

This work was financially supported by the National Key Research and Development Program of China (2021YFE0110400); the Key Collaborative Research Program of the Alliance of International Science Organization (ANSO-CR-KP-2020-13), the National Natural Science Foundation of China (52072387).

Author Contributions

Hongyun Xue prepared samples, tested properties, and wrote the manuscript. Jing Sun supervised this project. Gansheng Shi, Guanhong Lu, Xinhong Xu, Xiaomeng Ren, Xiao Wang, Xiaofeng Xie, Jing Sun, and Yan Wang provided valuable comments, and revised the manuscript. All authors have given approval to the final version of the manuscript.

Appendix A. Supplementary data

Supplementary data to this article can be found online at https://doi.org/10.1016/j.jphotochem.2023.115252.

References

[1] S.-K. Song, Z.-H. Shon, Y.-H. Kang, K.-H. Kim, S.-B. Han, M. Kang, J.-H. Bang, I. Oh, Source apportionment of VOCs and their impact on air quality and health in the megacity of Seoul, Environ. Pollut. 247 (2019) 763–774.

[2] Z. Wang, Z. Shi, F. Wang, W. Liang, G. Shi, W. Wang, D. Chen, D. Liang, Y. Feng, A. G. Russell, Implications for ozone control by understanding the survivor bias in observed ozone-volatile organic compounds system, npj Climate and Atmospheric, Science 5 (2022).

[3] C. Zhang, J. Qin, C. Yang, Y. Hu, Sulfur-vacancy-rich ZnS/CdIn2S4 heterojunction for efficient photocatalytic selective oxidation of toluene to benzaldehyde, J. Photochem. Photobiol. A Chem. 444 (2023).

[4] Y. Peng, X. Wei, Y. Wang, W. Li, S. Zhang, J. Jin, Metal-Organic Framework Composite Photothermal Membrane for Removal of High-Concentration Volatile Organic Compounds from Water via Molecular Sieving, ACS Nano 16 (2022) 8329–8337.

[5] X.H. Tai, C.W. Lai, T.C.K. Yang, C.-Y. Chen, A.H. Abdullah, K.M. Lee, J.C. Juan, Effective oxygenated boron groups of boron-doped photoreduced graphene oxide for photocatalytic removal of volatile organic compounds, J. Environ. Chem. Eng. 10 (2022).

[6] B. Liu, Z. Hu, B. Zhang, B. Liu, G. Li, T. Zhang, J. Ji, K. Li, W. Dai, J. Zhang, H. Huang, Deep Photocatalytic Oxidation of Aromatic VOCs on ZnSn LDH: Promoting Role of Electron Enrichment of Surface Hydroxyl, ACS Catal. 13 (2023) 7857–7867.

[7] W. Zhang, G. Li, H. Liu, J. Chen, S. Ma, M. Wen, J. Kong, T. An, Photocatalytic degradation mechanism of gaseous styrene over Au/TiO2@CNTs: Relevance of superficial state with deactivation mechanism, Appl Catal B 272 (2020).

[8] S. Verma, K. Vikrant, K.-H. Kim, Optimization of process variables for the concurrent removal of aliphatic and aromatic volatile organic compounds over a copper impregnated titanium dioxide photocatalyst, Environmental Science, Nano 10 (2023) 2035–2052.

[9] H. Liu, Y. Li, M. Xiang, H. Zeng, X. Shao, Single-layered MoS2 directly grown on rutile TiO2(110) for enhanced interfacial charge transfer, ACS Nano 13 (2019) 6083–6089.

[10] M. Xue, X. Wang, X. Li, L. Qin, S. Han, S.-Z. Kang, C3N4 nanosheets loaded with the CuWO4 activated NiS co-catalyst: A stable noble metal-free photocatalyst with dramatic photocatalytic activity for H2 generation and high salinity tolerant, J. Photochem. Photobiol. A Chem. 405 (2021).

[11] Y. Li, M.Q. Zhang, Y.F. Liu, Y.X. Sun, Q.H. Zhao, T.L. Chen, Y.F. Chen, S.F. Wang, In Situ Construction of Bronze/Anatase TiO(2) Homogeneous Heterojunctions and Their Photocatalytic Performances, Nanomaterials (basel) 12 (2022).

[12] N. Sedaghati, A. Habibi-Yangjeh, M. Pirhashemi, S. Asadzadeh-Khaneghah, S. Ghosh, Integration of BiOI and Ag3PO4 nanoparticles onto oxygen vacancy rich-TiO2 for efficient visible-light photocatalytic decontaminations, J. Photochem. Photobiol. A Chem. 400 (2020).

[13] P. Chang, Y. Wang, Y. Wang, Y. Zhu, Current trends on In2O3 based heterojunction photocatalytic systems in photocatalytic application, Chem. Eng. J. 450 (2022).

[14] Y. Kamakura, C. Suppaso, I. Yamamoto, R. Mizuochi, Y. Asai, T. Motohashi, D. Tanaka, K. Maeda, Tin(II)-based metal-organic frameworks enabling efficient, selective reduction of CO(2) to formate under visible light, Angew. Chem. Int. Ed. Engl. 62 (2023) e202305923.

[15] S. Zhao, Y. Wang, J. Dong, C.-T. He, H. Yin, P. An, K. Zhao, X. Zhang, C. Gao, L. Zhang, J. Lv, J. Wang, J. Zhang, A.M. Khattak, N.A. Khan, Z. Wei, J. Zhang, S. Liu, H. Zhao, Z. Tang, Ultrathin metal–organic framework nanosheets for electrocatalytic oxygen evolution, Nat. Energy 1 (2016).

[16] Q. Lan, S. Jin, B. Yang, Z. Zhang, X. Li, H. Xie, X. Jin, H. Zhang, Q. Zhao, Filling polyoxoanions into MIL-101(Fe) for adsorption of organic pollutants with facile and complete visible light photocatalytic decomposition, Molecules 27 (2022).

[17] Y. Wan, Y. Miao, T. Qiu, D. Kong, Y. Wu, Q. Zhang, J. Shi, R. Zhong, R. Zou, Tailoring amine-functionalized Ti-MOFs via a mixed ligands strategy for high-efficiency CO(2) Capture, Nanomaterials (basel) 11 (2021).

[18] Z. Zhou, W. Wang, H. Shi, L. Liu, T. Ma, T. Li, W. Huang, Y. Liu, S. Liu, Z. Xu, Metal-organic framework based polymer fibers: review on synthesis and applications, Advanced Materials Technologies 8 (2023).

[19] X. Deng, S.-L. Zheng, Y.-H. Zhong, J. Hu, L.-H. Chung, J. He, Conductive MOFs based on thiol-functionalized linkers: challenges, opportunities, and recent advances, Coord. Chem. Rev. 450 (2022).

[20] T. Xia, Y. Lin, W. Li, M. Ju, Photocatalytic degradation of organic pollutants by MOFs based materials: A review, Chin. Chem. Lett. 32 (2021) 2975–2984.

[21] J. Chen, Y. Zhu, S. Kaskel, Porphyrin-Based Metal-Organic Frameworks for Biomedical Applications, Angew. Chem. Int. Ed. Engl. 60 (2021) 5010–5035.

[22] Q. Xia, H. Wang, B. Huang, X. Yuan, J. Zhang, J. Zhang, L. Jiang, T. Xiong, G. Zeng, State-of-the-Art Advances and Challenges of Iron-Based Metal Organic Frameworks from Attractive Features, Synthesis to Multifunctional Applications, Small 15 (2019) e1803088.

[23] D. Wang, R. Huang, W. Liu, D. Sun, Z. Li, Fe-Based MOFs for Photocatalytic CO2 Reduction: Role of Coordination Unsaturated Sites and Dual Excitation Pathways, ACS Catal. 4 (2014) 4254–4260.

[24] V. Sharma, M. Feng, Water depollution using metal-organic frameworks-catalyzed advanced oxidation processes: A review, J. Hazard. Mater. 372 (2019) 3–16.

[25] J. Flores, R. Delgado-García, M. Sánchez-Sánchez, Semiamorphous Fe-BDC: The missing link between the highly-demanded iron carboxylate MOF catalysts, Catal. Today 390–391 (2022) 237–245.

[26] J. Duan, S. Chen, C. Zhao, Ultrathin metal-organic framework array for efficient electrocatalytic water splitting, Nat. Commun. 8 (2017) 15341.

[27] A. Idris, X. Jiang, J. Tan, Z. Cai, X. Lou, J. Wang, Z. Li, Dye-Sensitized Fe-MOF nanosheets as Visible-Light driven photocatalyst for high efficient photocatalytic CO2 reduction, J. Colloid Interface Sci. 607 (2022) 1180–1188.

[28] G. Lu, X. Wang, Y. Wang, G. Shi, X. Xie, J. Sun, Anti-oxidative microstructure design of ultra-stable N-TiO2 composite for the gaseous photodegradation reactions, Chem. Eng. J. 408 (2021), 127257.

[29] K. Rui, G. Zhao, Y. Chen, Y. Lin, Q. Zhou, J. Chen, J. Zhu, W. Sun, W. Huang, S. X. Dou, Hybrid 2D dual-metal–organic frameworks for enhanced water oxidation catalysis, Adv. Funct. Mater. 28 (2018) 1801554.
[30] Y. Gong, B. Yang, H. Zhang, X. Zhao, A g-C3N4/MIL-101(Fe) heterostructure composite for highly efficient BPA degradation with persulfate under visible light irradiation, J. Mater. Chem. A 6 (2018) 23703–23711.
[31] Y. Guo, C. Feng, S. Qiao, S. Wang, T. Chen, L. Zhang, Y. Zhao, J. Wang, Magnetic Fe3O4-encapsulated VAN@MIL-101(Fe) with mixed-valence sites and mesoporous structures as efficient bifunctional water splitting photocatalysts, Nanoscale 12 (2020) 12551–12560.
[32] R. Liang, F. Jing, L. Shen, N. Qin, L. Wu, MIL-53(Fe) as a highly efficient bifunctional photocatalyst for the simultaneous reduction of Cr(VI) and oxidation of dyes, J. Hazard. Mater. 287 (2015) 364–372.
[33] X.-Q. Qiao, Z.-W. Zhang, D.-F. Hou, D.-S. Li, Y. Liu, Y.-Q. Lan, J. Zhang, P. Feng, X. Bu, Tunable MoS2/SnO2 P-N Heterojunctions for an Efficient Trimethylamine Gas Sensor and 4-Nitrophenol Reduction Catalyst, ACS Sustain. Chem. Eng. 6 (2018) 12375–12384.
[34] J. Zhang, D. Yang, J. Shi, Z. Wang, W. Zhu, Y. Wang, Z. Chen, Improving oxygen evolution activity by constructing a perylene imide based Z-scheme heterojunction, J. Mater. Chem. A 10 (2022) 14513–14528.
[35] L. Huang, J. Liu, Y. Li, L. Yang, C. Wang, J. Liu, H. Li, L. Huang, Enhancement of photocatalytic activity of Z-scheme BiO2-x/BiOI heterojunction through vacancy engineering, Appl. Surf. Sci. 555 (2021), 149665.
[36] J. Raskó, J. Kiss, Adsorption and surface reactions of acetaldehyde on TiO2, CeO2 and Al2O3, Appl. Catal. A 287 (2005) 252–260.
[37] Q. Zeng, X. Xie, X. Wang, Y. Wang, G. Lu, D.Y.H. Pui, J. Sun, Enhanced photocatalytic performance of Ag@TiO2 for the gaseous acetaldehyde photodegradation under fluorescent lamp, Chem. Eng. J. 341 (2018) 83–92.